

Identifying Fibre Orientations for Fracture Process Zone Characterisation in Scaled Centre-Notched Quasi-Isotropic Carbon/Epoxy Laminates with a Convolutional Neural Network

Xiaodong Xu^{a,b,*}, Aser Abbas^c, Juhyeong Lee^{d,**}

^a*Department of Engineering Design and Mathematics, University of the West of
England, Coldharbour Lane, Frenchay Campus, Bristol BS16 1QY, UK*

^b*Bristol Composites Institute, University of Bristol, University Walk, Bristol BS8 1TR,
UK*

^c*Department of Civil and Environmental Engineering, Utah State University, Logan, UT
84322-4110, USA*

^d*Department of Mechanical and Aerospace Engineering, Utah State University, Logan,
UT 84322-4130, USA*

Abstract

This paper presents a novel X-ray Computed Tomography (CT) image analysis method to characterise the Fracture Process Zone (FPZ) in scaled centre-notched quasi-isotropic carbon/epoxy laminates. A total of 61 CT images of a small specimen were used to fine-tune a pre-trained Convolutional Neural Network (CNN) (i.e., VGG16) to classify fibre orientations. The proposed CNN model achieves a 100% accuracy when tested on the CT images of the same scale as the training set. However, the accuracy drops to a maximum of 84% when tested on unlabelled images of the specimens having larger scales potentially due to their lower resolutions. Another code was developed to

*Corresponding author

**Corresponding author

Email addresses: xiaodong.xu@uwe.ac.uk (Xiaodong Xu), juhyeong.lee@usu.edu (Juhyeong Lee)

automatically measure the size of the FPZ based on the CNN identified 0° plies in the largest specimen which agrees well with the manual measurement (on average within 3.3%). The whole classification and measurement process can be automated without human intervention.

Keywords: Laminates; Fracture; X-ray Computed Tomography; Convolutional Neural Network

1. Introduction

A size effect describes the change of strength with specimen dimensions [1]. It has significant implications on the strength prediction of full-scale aerospace structures, which were proven to be challenging [2, 3]. Previously, in-plane
5 scaled centre-notched quasi-isotropic (QI) carbon/epoxy specimens were tested, and the tensile strength was found to decrease with increasing specimen dimensions [4]. The size effect was associated with a Fracture Process Zone (FPZ) ahead of the centre-notch tips. It is crucial to characterise the FPZ in order to explain the size effect in QI laminates.

10 FPZ was studied by using a variety of techniques including Digital Image Correlation (DIC) [5, 6, 7], and X-ray Computed Tomography (CT) [4, 8, 9]. DIC can generate surface strain fields automatically, which is then associated with the size of FPZ via some assumptions, e.g., force equilibrium being achieved at the FPZ boundary in [6]. Compared with DIC, CT scanning
15 can objectively quantify internal damage, such as in 0° plies, and accurately determine the size of the FPZ. By using CT scans, it was found that the size of the FPZ, which was quantified by the fibre breakage length in the 0° plies, initially scaled with the notch size and then approached a plateau

at larger scales, leading to a change of scaling law [4]. However, processing
20 CT data is a time-consuming manual process. Automation of CT analysis
for FPZ characterisation can potentially further promote the adoption of CT
scanning.

Convolutional Neural Networks (CNN) are an excellent tool for computer
vision tasks like image recognition and classification. CNNs are usually built
25 using three types of layers: *i*) convolutional layers, *ii*) sub-sampling layers,
and *iii*) fully connected layers. The convolutional layers employ a set of filter
masks, also called feature detectors, to capture the relevant patterns (*i.e.*,
feature maps) in the dataset images. Once the relevant features of the images
are detected, sub-sampling (or pooling) layers are usually utilized to decrease
30 the feature maps' spatial resolution, which in turn reduces the reliance on
precise positioning within feature maps produced by the convolutional lay-
ers. Disregarding the exact position of features within a feature map while
maintaining the relative position of features with respect to each other al-
lows for a better CNN performance on inputs that relatively differ from the
35 training data. The final convolutional or sub-sampling layer is flattened and
connected to fully connected layer(s) to perform the classification task.

CNNs have been used to analyse images of advanced materials, such as a
bicontinuously nanostructured copolymer [10], and 3D-printed metal [11] to
characterise cracks. Trained by finite element simulations, these CNNs de-
40 rived accurate fracture properties, including crack length and fracture tough-
ness. CNNs have been widely applied to medical CT analysis, such as for
intraoperative imaging, to improve surgical precision as reviewed by Alam
et al. [12]. However, only a few articles were published on CT analysis of

advanced composites using CNNs. For example, Yang et al. [13] adopted a U-
45 net CNN to reconstruct a rubber composite structure from only tens of μ CT
images. Chen et al. [14] also adopted a U-net deep CNN to create digital ma-
terial twins for woven ceramic-matrix composites from μ CT images. Tian et
al. [15] used a mask and regional CNN to detect local cracks from CT images
of concrete. A deep CNN was also used to detect surface or near-surface
50 defects in composites from X-rays [16]. Some work on characterization of
individual fiber orientation has been done using dictionary-learning [17] in
which a segmentation method could accurately extract individual fibres from
low contrast X-ray scans of composites with high fibre volume fraction. How-
ever, classification of fibre orientations using CNNs from CT images has not
55 been done. This is extremely useful for the determination of fracture prop-
erties of composites, such as the size of the FPZ.

This paper presents a novel CT analysis method using a CNN for classi-
fication of fibre orientations and then another code to measure FPZs. The
proposed workflow is established to automatically measure the FPZ size in
60 centre-notched QI carbon/epoxy laminates in two steps. First, a pre-trained,
fine-tuned VGG16 CNN was trained using labelled CT images of the centre-
notched specimens from interrupted tests at 95% of average failure load.
Then, the CNN was applied to the unlabelled CT images of the other centre-
notched specimens having different scales to classify their fibre orientations.
65 A test accuracy of 100% for the former and a maximum prediction accuracy
of 84% for the latter were achieved. After the 0° plies were identified, the
size of the FPZ in the largest centre-notched specimen was automatically
measured to understand the size effect by using an image analysis workflow.

To the author’s best knowledge, this paper is the first to use a CNN for the
70 classification of fibre orientations in multi-directional composites from CT
images. The present method can potentially automate CT analyses for FPZ
evolution with notches. In doing so, it can improve accuracy and efficiency
and reduce potential human errors.

2. Experiments

75 A schematic of the in-plane scaled centre-notched QI specimens is shown
in Figure 1(a). The specimens with a notch length of $C = 3.2$ mm is referred
to as the baseline, $C = 6.4$ mm as Scale 2, $C = 12.7$ mm as Scale 4 and $C =$
25.4 mm as Scale 8. The schematic of the largest centre-notched specimens
with a notch length of $C = 50.8$ mm (Scale 16) is shown in Figure 1(b).
80 Only their width and notch length are doubled from the Scale 8 specimens,
while their gauge length remains the same. Scale 16 specimens were not fully
scaled due to limitations of the facilities. It was found that the specimens
with a halved gauge length of the baseline specimens had a similar tensile
strength within 3% [4].

85 The material used was HexPly[®] (Hexcel, US) IM7/8552 carbon-epoxy
unidirectional pre-preg with a cured nominal ply thickness of 0.125 mm.
The stacking sequence was $[45/90/-45/0]_{4s}$, for all the sizes. The nominal
specimen thickness was 4 mm. The centre notches were cut with a 1 mm end
mill on a Computer Numerical Controlled milling machine. Then the notch
90 tips were manually extended by using 0.25 mm-wide piercing saw blades.

250kN Instron and 500kN Dartec hydraulic-driven test machines were
used. The scaled specimens were tested under tension using displacement

control with scaled loading rates for different gauge lengths, e.g., 0.25 mm/min for the baseline, 0.5 mm/min for Scale 2, 1 mm/min for Scale 4, 2 mm/min
95 for Scale 8 and Scale 16. Interrupted tests in which the tests were stopped at 95% of the average failure load were carried out. The tensile test results were documented in by Xu et al. [4].

A single specimen from each size was examined by CT scanning to measure the FPZ, so a total of five specimens were scanned. The specimen from
100 the interrupted tests were soaked in a bath of zinc iodide penetrant for three days. A Nikon XT H 225 ST CT scanner was used to scan the specimens from interrupted tests. The scanner has a 3 μm focal spot size, but the spatial resolution varies with the specimen size. For example, the CT images of the scaled centre-notched specimens reported by Xu et al. [4] had a pixel
105 size of 18 μm for the baseline, 20 μm for Scale 2, 47 μm for Scale 4 and 71 μm for Scale 8. The CT images of the largest Scale 16 specimens were not reported by Xu et al. [4] because they were too large for the CT scanner to generate quality images. In this paper, the largest Scale 16 specimen from the interrupted test for CT scanning was cut down to a narrower strip
110 parallel to the centre notch, so the X-ray source could be placed closer to the notch tips to achieve a pixel size of 106 μm . The edges of the strip were kept away from the centre notch, so no further damage was introduced to the existing FPZ at the notch tip as shown in Figure 2. The 3D CT volumes were segmented into 2D CT images for each ply through the specimen thickness
115 in VG Studio Max (Volume Graphics, Germany). The previously labelled CT images from the single CT scan of the Scale 2 specimen were used for training, validation, and testing of the CNN for image classification. Then

the CNN was applied to the unlabelled CT images of Scale 4, Scale 8, and the new Scale 16 specimens to classify their fibre orientations. The details
120 are explained in Section 4.1.

3. CNN Methodology

Training a CNN from scratch to obtain a high classifier accuracy requires significantly more training data than is feasible in this case due to the expensive nature and the human resources necessary to run the CT scans. Data
125 augmentation and transfer learning were used in this paper to overcome the relatively limited training set size. Additionally, the CT images were standardized by making the mean of the entire dataset equal to zero and the standard deviation equal to one. Transfer learning allows for good accuracy when dealing with small datasets by taking a pre-trained Neural Network and
130 re-purposing its learned features and weights to model a different dataset. The ability of several well-known CNN architectures and weights to fit and classify our dataset was investigated (e.g., ResNet50 [18], InceptionV3 [19], and VGG16 [20]). A fine-tuned version of VGG16 yielded the best accuracy in our case, with a 100% ability to provide the correct classification for the
135 considered testing set using labelled CT images.

VGG16 won the first and second places in the ImageNet large-scale visual recognition competition (ILSVRC) 2014 in the localization and the classification tasks, respectively. The ImageNet dataset used in training VGG16 includes over 14 million images belonging to around 22 thousand
140 categories [20, 21]. VGG16 comprises 16 trainable layers interspersed with sub-sampling layers, as shown in Figure 3, and is considered as one of the

excellent vision model architectures. In this paper, the pre-trained weights of the convolutional layers have been maintained while optimizing the weights of the two last fully connected layers to model the dataset. A stochastic gradient
145 descent optimizer was adopted with a learning rate of 10^{-3} , a decay of 10^{-6} , and a 0.9 momentum paired with Nesterov’s accelerated gradient [22, 23].

4. Results

4.1. Classification of fibre orientations using a CNN

The objective of the proposed CNN is to classify fibre orientations in
150 the in-plane scaled center-notched specimens into three classes, 0° , 45° , and 90° plies, based on CT images from the interrupted tests according to the flowchart in Figure 6. A total of 61 labelled CT images from the Scale 2 interrupted test were used for the *i*) training, *ii*) validation and *iii*) testing of the CNN. All above images were augmented by horizontal flipping, rotating,
155 and shifting the original CT images in each set using Keras’s image data generator class [22]. The baseline specimen has a different damage pattern in the centre 0° ply compared to other sizes, so it is not used in the CNN. The Scale 2 images have better quality than the even larger scales, so are chosen for training. The Scale 2 images were approximately split into an 80%
160 training set and a 20% validation & testing set. Specifically, the training set comprised 12 CT images of the 0° plies, 25 of the 45° plies, and 12 of the 90° plies. The validation & testing set contained 4 CT images of the 0° , 4 of the 45° , and 4 of the 90° plies. Each ply was sliced once. The CNN reached a 100% model accuracy after 20 epochs, based on a categorical
165 cross-entropy loss function. Figure 4 contains the accuracy (left) and loss

function value (right) of a trained model showing a 100% model accuracy. The corresponding confusion matrix normalized by the numbers of tested images for each considered fibre orientation is shown in Figure 5. It shows fibre orientation prediction; diagonal-terms all being 1 mean that the trained
170 model identified all fibre orientation correctly. They show that the predicted fibre orientations agree extremely well with the true fibre orientations within the training set. The total run time was 1.7 seconds and the time per step at the final epoch was 0.27 seconds, demonstrating the computational efficiency of the current CNN model.

175 Once training, validation, and testing were completed based on the Scale 2 CT images, the CNN was also applied to Scales 4, 8, and the new Scale 16 CT images to predict their fibre orientations. The prediction accuracy dropped to 83.9% for Scale 4, 62.6% for Scale 8, and 60.1% for Scale 16 as shown in Figure 7. This means that when the scale of the target CT images
180 is closer to that of the training dataset, the prediction accuracy is higher. However, it was preferred to use the CNN trained by the Scale 2 CT images to identify the 0° plies of the largest Scale 16 specimen for two practical reasons: *i*) this proposed bottom-up approach is more in line with the test pyramid approach for real-world applications and *ii*) the new FPZ measurements for
185 Scale 16 specimens are more representative of the material properties since the FPZ from the smaller specimens are not fully developed [4].

4.2. FPZ characterisation

The FPZ size is defined as the average horizontal distance between the furthest fibre breakage point to the notch tip in the single 0° plies. The
190 furthest fibre breakage point is often marked by the last 0° split in the speci-

men, but practically represented the furthest pixel in black in the CT images. Previously, the size of FPZ was measured manually for the baseline, Scale 2, Scale 4, and Scale 8 specimens as shown in Figure 8 [4]. In the current study, the FPZ measurements were done both manually and automatically based
195 on the new set of CT images from the Scale 16 specimen. A spatial scale was printed on the images during the CT analysis (Figure 9). After the CNN was trained and used to identify the 0° plies, a workflow was developed to automatically post-process the CT images by isolating the spatial scale and the crack to measure its dimensions as shown in Figure 6. First, the images were
200 cropped and resized while preserving the original images' aspect ratio. The crack and spatial scale's colour gamut was then isolated from the rest of the image. The scale to pixel ratio was then calculated from the filtered image, which was then used to calculate the size of the FPZ based on the number of pixels occupied by the crack. As a comparison, manual measurements were
205 also done using the software *Image J* (National Institutes of Health, US) by comparing the number of pixels for the FPZ and that for the scale.

The automatic measurements of the FPZ are compared with the manually measured values in Table 1. From the first 9 images out of the total 12 considered, the automatically measured FPZ size is 2.79 mm, with an average
210 relative percentage error of 3.3% from the manual measurement. The last three measurements, however, show a large discrepancy. The reason for this is because some excessive dye penetrant remains in the pre-existing crack tip, which misleads the code to believe that it is part of the FPZ (Figure 10). These three measurements are an artifact of the image processing analysis,
215 so they are excluded when calculating the size of the FPZ.

5. Discussion

One may argue that this satisfactory result (a 100% model accuracy) emanates from over-interpretation (or over-fitting) of the training dataset. This may be true for a small dataset (≤ 100 data) used for training. In this work, a VGG16 is a backbone CNN architecture and fine-tuned with optimizing the weights of only last fully connected layers (Figure 3). As previously stated, data augmentation and transfer learning was applied to try to avoid potential over-fitting of the model. The CNN model is currently being improved with cross-validation, feature selection, and regularization techniques to simplify its architecture, thus overcoming potential over-fitting issue.

It is not surprising that the accuracy drops, depending on how different the scale of the target CT images is from the training dataset. The CNN generally predicts the fibre orientations from the CT images of the relatively smaller specimens (Scale 4) more accurately than from the larger specimens (Scales 8 and 16). This is partially due to noisier CT data and poorer CT image quality at the larger scales. More work is needed to improve the proposed CNN prediction accuracy when dealing with the unlabelled CT images of different specimen sizes.

A question that arises from this paper is, “Human vs. Machine learning, which is better?”. When identifying the fibre orientations in the centre-notched QI carbon/epoxy laminates, the CNN initially showed a high accuracy level. However, the code showed limitations when measuring the FPZ from the identified 0° plies, such as not recognizing the excessive dye penetrant. This illustrates that the second automated step for FPZ measurement

could be further improved, e.g., by creating a mask using a threshold optimized for each CT image.

The new CT images confirm that the measured FPZ size of the Scale 16 specimens ($C = 50.8$ mm) does not double when compared to the previously
245 reported 2.28 mm for the Scale 8 specimens ($C = 25.4$ mm) [4]. Instead, it approaches an approximately constant size while the notched strength approaches a fracture-mechanics scaling asymptote [4].

6. Conclusions

A Convolutional Neural Network (CNN) has been successfully imple-
250 mented for in-plane scaled centre-notched carbon/epoxy quasi-isotropic (QI) laminates to classify fibre orientations based on X-ray Computed Tomography (CT) images. It achieved a 100% test accuracy on the labelled Scale 2 CT images (the same scale as the training set) and a maximum prediction accuracy of 84% using the unlabelled CT images of the other sized spec-
255 imens (Scales 4, 8 and 16). After the 0° plies were identified, the size of the FPZ from the new CT images of the Scale 16 specimens was automatically measured using another newly developed image processing code. The automatically measured FPZ size agrees well with the manually measured average value using *Image J* with an average relative error of 3.3%. The
260 current method enables the automation of FPZ characterisation from CT images, potentially eliminating human interventions while maintaining good accuracy.

7. Acknowledgements

This work was financially supported by the Vice Chancellor's Early Career
265 Research Development Award at the University of the West of England,
UK. This work was also partially supported by New Faculty Research Start-
up Funding from the Utah State University Office of Research, USA. The
authors thank Professor Michael R. Wisnom from the University of Bristol
for his valuable advice.

270 8. Data availability

The raw/processed data required to reproduce these findings cannot be
shared at this time as the data also forms part of an ongoing study.

References

- [1] Wisnom MR. Size effects in the testing of fibre-composite materials.
275 Composites Science and Technology 1999;59:1937–57. doi:[10.1016/
S0266-3538\(99\)00053-6](https://doi.org/10.1016/S0266-3538(99)00053-6).
- [2] Xu X, Takeda SI, Aoki Y, Hallett S, Wisnom M. Predicting notched
tensile strength of full-scale composite structures from small coupons
using fracture mechanics. Composite Structures 2017;180. doi:[10.1016/
280 j.compstruct.2017.08.026](https://doi.org/10.1016/j.compstruct.2017.08.026).
- [3] Bergan A, Bakuckas J, Awerbuch J, Tan TM. Assessment of damage
containment features of a full-scale prseus fuselage panel. Composite
Structures 2014;113:174–85. doi:[10.1016/j.compstruct.2014.03.011](https://doi.org/10.1016/j.compstruct.2014.03.011).

- 285 [4] Xu X, Wisnom M, Mahadik Y, Hallett S. An experimental investigation into size effects in quasi-isotropic carbon/epoxy laminates with sharp and blunt notches. *Composites Science and Technology* 2014;100. doi:[10.1016/j.compscitech.2014.06.002](https://doi.org/10.1016/j.compscitech.2014.06.002).
- [5] Catalanotti G, Camanho PP, Xavier J, Dávila CG, Marques AT. Measurement of resistance curves in the longitudinal failure of composites using digital image correlation. *Composites Science and Technology* 290 2010;70:1986–93. doi:[10.1016/j.compscitech.2010.07.022](https://doi.org/10.1016/j.compscitech.2010.07.022).
- [6] Zobeiry N, Vaziri R, Poursartip A. Characterization of strain-softening behavior and failure mechanisms of composites under tension and compression. *Composites Part A: Applied Science and Manufacturing* 295 2015;68:29–41. doi:[10.1016/j.compositesa.2014.09.009](https://doi.org/10.1016/j.compositesa.2014.09.009).
- [7] Bergan A, Dávila C, Leone F, Awerbuch J, Tan TM. A mode I cohesive law characterization procedure for through-the-thickness crack propagation in composite laminates. *Composites Part B: Engineering* 2016;94:338–49. doi:[10.1016/j.compositesb.2016.03.071](https://doi.org/10.1016/j.compositesb.2016.03.071).
- 300 [8] Xu X, Wisnom MR, Mahadik Y, Hallett SR. Scaling of fracture response in over-height compact tension tests. *Composites Part A: Applied Science and Manufacturing* 2015;69:40–8. doi:[10.1016/j.compositesa.2014.11.002](https://doi.org/10.1016/j.compositesa.2014.11.002).
- [9] Tan JL, Deshpande VS, Fleck NA. Failure mechanisms of a notched CFRP laminate under multi-axial loading. *Composites Part A: Applied Science* 305

and Manufacturing 2015;77:56–66. doi:[10.1016/j.compositesa.2015.06.005](https://doi.org/10.1016/j.compositesa.2015.06.005).

- [10] Jin H, Jiao T, Clifton RJ, Kim KS. Dynamic fracture of a bicontinuously nanostructured copolymer: A deep-learning analysis of big-
310 data-generating experiment. Journal of the Mechanics and Physics of Solids 2022;164:104898. doi:<https://doi.org/10.1016/j.jmps.2022.104898>.
- [11] Niu S, Srivastava V. Simulation trained cnn for accurate embedded crack
315 length, location, and orientation prediction from ultrasound measurements. International Journal of Solids and Structures 2022;242:111521. doi:<https://doi.org/10.1016/j.ijsolstr.2022.111521>.
- [12] Alam IS, Steinberg I, Vermesh O, van den Berg NS, Rosenthal EL, van Dam GM, et al. Emerging Intraoperative Imaging Modalities to Improve Surgical Precision. MOLECULAR IMAGING AND BIOLOGY
320 2018;20(5):705–715. doi:[10.1007/s11307-018-1227-6](https://doi.org/10.1007/s11307-018-1227-6).
- [13] Yang H, Wang W, Shang J, Wang P, Lei H, sen Chen H, et al. Segmentation of computed tomography images and high-precision reconstruction of rubber composite structure based on deep learning. Composites Science and Technology 2021;213:108875. doi:<https://doi.org/10.1016/j.compscitech.2021.108875>.
325
- [14] Chen Y, Chen Y, Wang D, Ai S. Generating 3D digital material twins for woven ceramic-matrix composites from μ CT images. Journal of

- the American Ceramic Society 2021;00:1–17. doi:<https://doi.org/10.1111/jace.18044>.
- 330 [15] Tian W, Cheng X, Liu Q, Yu C, Gao F, Chi Y. Meso-structure segmentation of concrete ct image based on mask and regional convolution neural network. *Materials & Design* 2021;208:109919. doi:<https://doi.org/10.1016/j.matdes.2021.109919>.
- [16] Gong Y, Shao H, Luo J, Li Z. A deep transfer learning model for
335 inclusion defect detection of aeronautics composite materials. *Composite Structures* 2020;252:112681. doi:<https://doi.org/10.1016/j.compstruct.2020.112681>.
- [17] Emerson MJ, Jespersen KM, Dahl AB, Conradsen K, Mikkelsen LP.
340 Individual fibre segmentation from 3d x-ray computed tomography for characterising the fibre orientation in unidirectional composite materials. *Composites Part A: Applied Science and Manufacturing* 2017;97:83–92. doi:<https://doi.org/10.1016/j.compositesa.2016.12.028>.
- [18] He K, Zhang X, Ren S, Sun J. Deep residual learning for image
345 recognition. 2016 IEEE Conference on Computer Vision and Pattern Recognition (CVPR) 2016;URL: <https://arxiv.org/abs/1512.03385v1>. doi:[10.1109/cvpr.2016.90](https://doi.org/10.1109/cvpr.2016.90).
- [19] Szegedy C, Vanhoucke V, Ioffe S, Shlens J, Wojna Z. Rethinking the
inception architecture for computer vision. 2016 IEEE Conference on
350 Computer Vision and Pattern Recognition (CVPR) 2016;doi:[10.1109/cvpr.2016.308](https://doi.org/10.1109/cvpr.2016.308).

- [20] Simonyan K, Zisserman A. Very Deep Convolutional Networks for Large-Scale Image Recognition 2014;[arXiv:1409.1556](#).
- [21] Deng J, Dong W, Socher R, Li LJ, Li K, Li FF. Imagenet: A large-scale hierarchical image database. 2009 IEEE conference on computer vision and pattern recognition 2009; 355
- [22] Chollet F. Xception: Deep learning with depthwise separable convolutions. In: 2017 IEEE Conference on Computer Vision and Pattern Recognition (CVPR). 2017, p. 1800–7. doi:[10.1109/CVPR.2017.195](#).
- [23] Ilya Sutskever James Martens GD, Hinton G. On the importance of initialization and momentum in deep learning. Proceedings of the 30th International Conference on Machine Learning 2013; 360

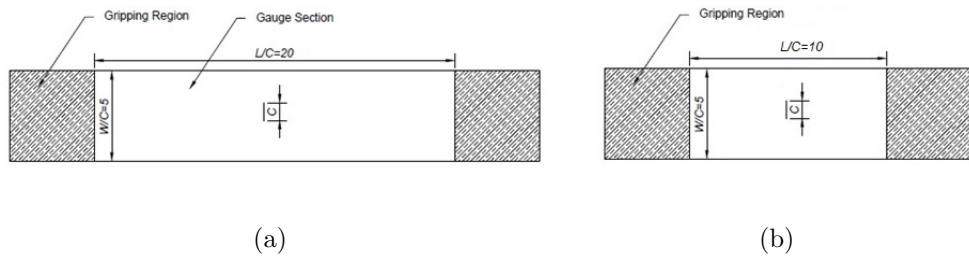


Figure 1: Schematic of (a) in-plane scaled centre-notched specimens with $C = 3.2$ to 25.4 mm and (b) largest specimen with $C = 50.8$ mm.

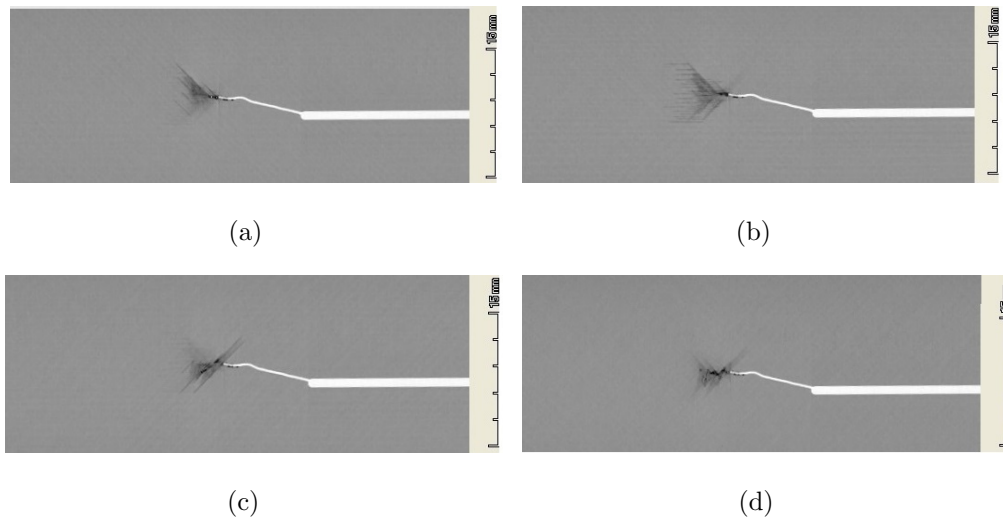


Figure 2: Typical CT images of Scale 16 specimen (a) 45° (b) 90° (c) -45° (d) 0° .

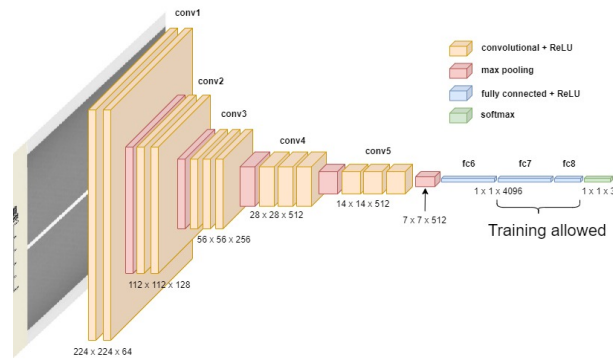


Figure 3: Proposed CNN architecture based on VGG16 with fine-tuning.

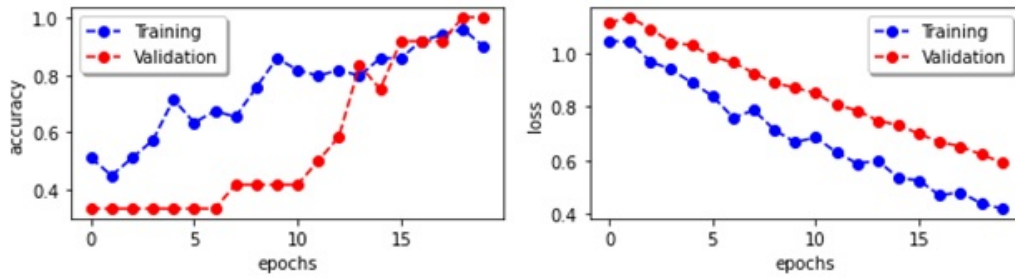


Figure 4: Proposed CNN model: model accuracy (left) and loss function value (right) over epochs.

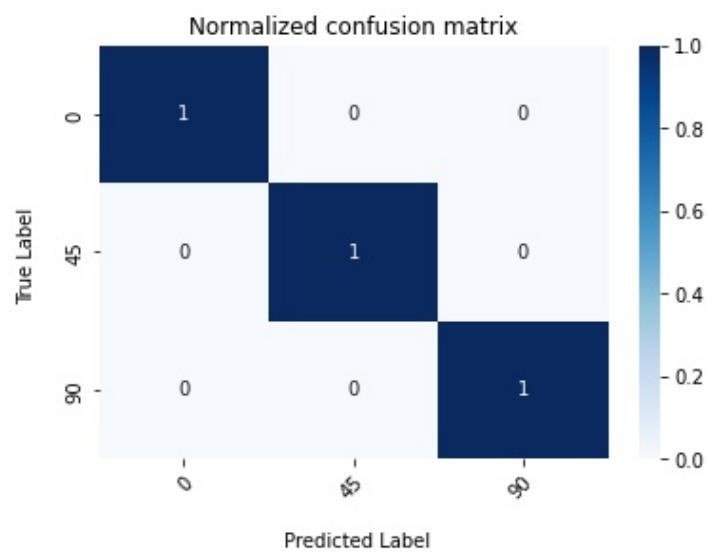


Figure 5: Normalized confusion matrix showing an excellent agreement between actual and predicted fibre orientations; diagonal terms being 1 means 100% accuracy, using the training dataset.

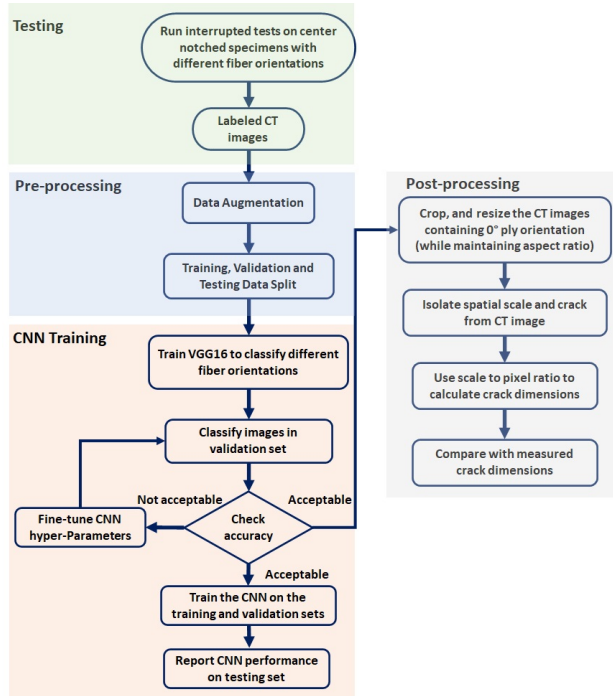


Figure 6: Two-step FPZ characterization process: CNN for fibre orientation identification and followed by automated post-processing for FPZ characterisation.

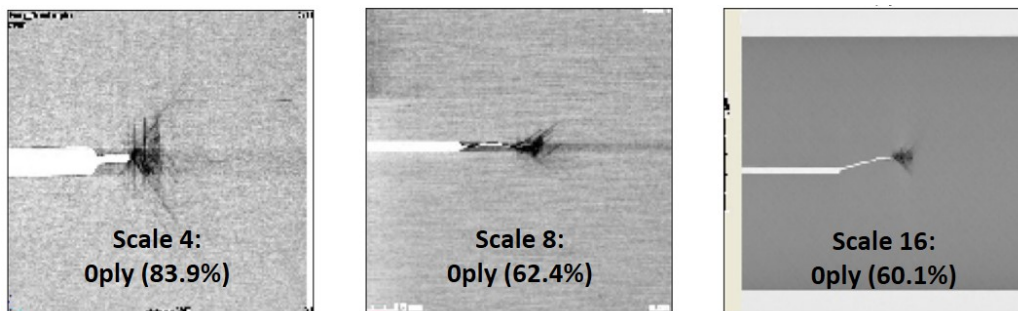


Figure 7: CNN model prediction accuracy on unlabelled CT images (not to scale).

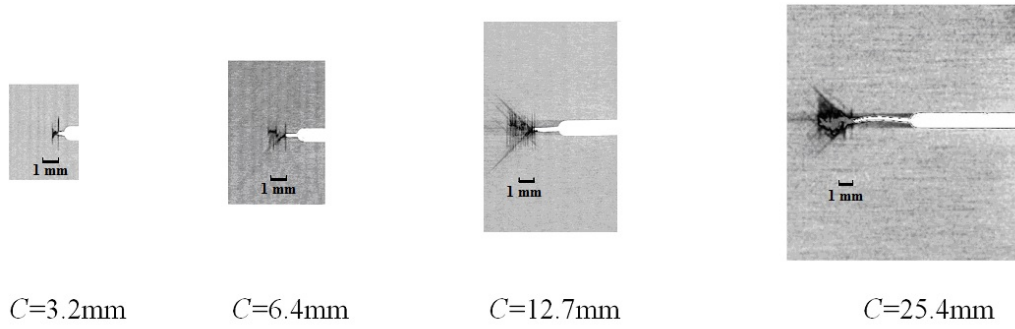


Figure 8: CT images of typical single 0° plies in scaled centre-notched specimens.

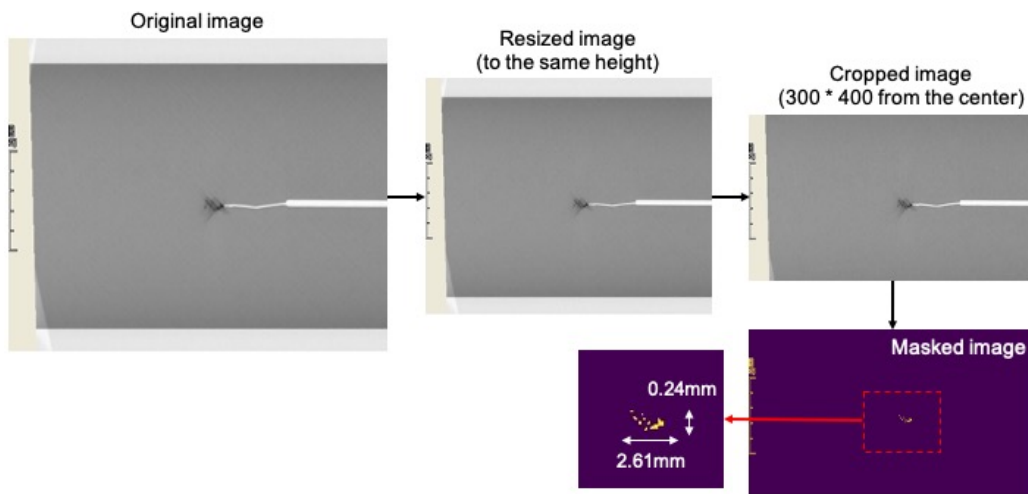


Figure 9: Automated crack measurements using the CT image of a 0° ply.

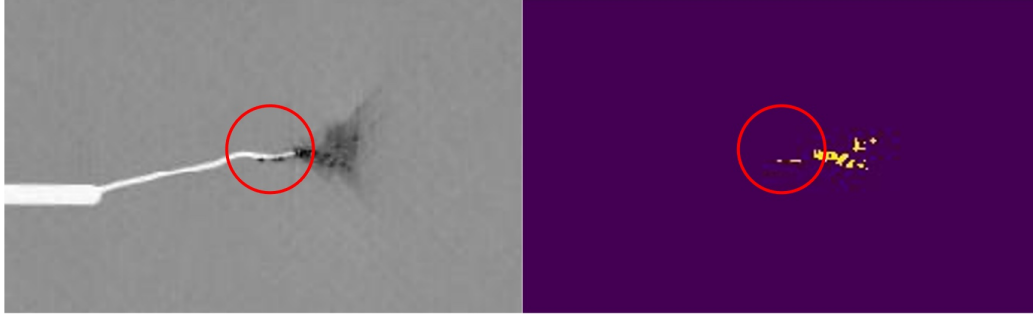


Figure 10: Over-estimated crack length due to excessive dye penetrant (in red circle).

Table 1: Comparison of FPZ measurements based on the 0° plies.

Image No.	Manual measurement	Automatic measurement	Error
1	2.85	2.79	-2.11%
2	2.74	2.71	-1.09%
3	2.74	2.81	2.55%
4	2.96	2.92	-1.35%
5	2.74	2.69	-1.85%
6	2.96	2.69	-9.12%
7	3.28	3.16	-3.66%
8	2.74	2.61	-4.74%
9	2.96	2.72	-8.11%
Mean	2.88	2.79	-3.27%
CV ^a	6.23%	5.92%	
10 ^b	2.96	4.99	68.8%
11 ^b	2.85	4.74	66.5%
12 ^b	3.39	5.34	57.3%

^a Coefficient of Variation

^b Measurements influenced by excessive dye penetrant are excluded